Journal of Non-Newtonian Fluid Mechanics 263 (2019) 24–32

Contents lists available at ScienceDirect

Journal of Non-Newtonian Fluid Mechanics

journal homepage: www.elsevier.com/locate/jnnfm

Local flow around a tiny bubble under a pressure-oscillation field in a viscoelastic worm-like micellar solution

Shuichi Iwata[a,*], Tsutomu Takahashi[b], Takashi Onuma[c], Ryo Nagumo[a], Hideki Mori[a]

[a] Department of Life Science and Applied Chemistry, Graduate School of Engineering, Nagoya Institute of Technology, Gokiso-cho, Showa-ku, Nagoya 466-8555, Japan
[b] Department of Mechanical Engineering, Graduate School of Engineering, Nagaoka University of Technology, 1603-1, Tomioka, Nagaoka, Niigata 940-2188, Japan
[c] Imaging division, Photron Limited, Kanda-Jinbocho 1-105 Chiyoda-ku, Tokyo 101-0051, Japan

ARTICLE INFO

Keywords:
Bubble
Pressure-oscillating
2D high-speed polarization camera
Viscoelastic fluid

ABSTRACT

The motion of a tiny air bubble in an aqueous solution of cetyl trimethyl ammonium bromide and sodium salicylate (CTAB/NaSal), which forms wormlike micelles, was observed using a high-speed polarization camera. Complex local flow is observed around the bubble surface because the bubble shape deforms repeatedly at 100 Hz. The camera can be used to measure the retardation distribution, which is related to the stress field around the bubble. Different retardation and orientation angle distributions were observed during the contraction and expansion phases. In the contraction phase, a strong retardation distribution appears at the tail of the cusped bubble. The occurrence of uniaxial elongation deformation is considered to be due to the negative wake because they are closely correlated. In contrast, a weak retardation distribution spreads at the upper side of the bubble during the expansion phase, where biaxial extensional deformation occurs due to expansion of the bubble surface. These significant changes in strong elastic stress distributions, which correspond to the orientation angle profiles, can result in increase of bubble rising velocities.

1. Introduction

One of the practical phenomena in many industrial processes is the rising of gas bubbles. There have been many fundamental studies related to the motion of gas bubbles; however, for the case of non-Newtonian fluids, interesting and unexpected observations remain unresolved [1]. For example, one well-known phenomenon in non-Newtonian fluids is the discontinuity in the bubble rising velocity. In a Newtonian fluid, the rising velocity of a gas bubble with a Reynolds number less than 1 (Stokes region [2]) is quadratically proportional to the bubble diameter, i.e., the gas bubble volume and rising velocity are related. However, for non-Newtonian liquids, many authors have reported a critical bubble volume, above which a rapid increase in the bubble rising velocity occurs. The rapid change of the bubble rising velocity is referred to as velocity jump.

Several groups have investigated the velocity jump in non-Newtonian fluids. For example, Astarita and Apuzzo [3] reported that the ratio of bubble rising velocity before and after the velocity jump is in the range of 2–6, depending on the polymer content in the solution. They argued that the velocity jump was the result of a transition from the Stokes region to the Hadamard region [4], i.e., a change from a rigid bubble interface to a free bubble interface. The velocity jump that results from such a change in boundary conditions could be up to 1.5 times. However, this transition cannot fully explain a six-fold increase in the bubble rising velocity.

Hassager [5] reported on the bubble rising velocity and the wake behind an air bubble in a non-Newtonian liquid, where laser Doppler anemometry was used to measure the liquid velocity. For small bubbles (with a volume smaller than the critical volume), the dominant flow in the wake behind the air bubble is towards the upper direction, i.e., the direction of rising. Such a wake is referred to as a positive wake and is similar to the flow of a bubble in Newtonian fluid. On the other hand, for large bubbles (with a volume larger than the critical volume), the flow is towards the lower direction, i.e., opposite to the bubble rising direction and thus termed a negative wake. In this case, the bubble shape has a cusped shape that seems to be sharpened at the tail of the bubble. To investigate the structure of a negative wake, Herrera-Velarde et al. [6] showed different types of wake behind a rising bubble before and after the critical volume using the particle image velocimetry (PIV) technique. Li and colleagues [7–9] used two practical methods, PIV and birefringence visualization. The latter method was performed by crossed Nicols measurements with two sheets of polarizer plate to visualize the stress field around the bubble. Moreover, a lattice Boltzmann (LB) simulation was used for the complex flow field, whereby they reported that the negative wake is related to the viscoelastic properties of the fluid. Pillapakkam et al. [10] indicated that a vortex ring

* Corresponding author.
E-mail address: iwa@nitech.ac.jp (S. Iwata).

https://doi.org/10.1016/j.jnnfm.2018.11.002
Received 3 August 2018; Received in revised form 2 November 2018; Accepted 6 November 2018
Available online 7 November 2018
0377-0257/© 2018 Elsevier B.V. All rights reserved.

Nomenclature

C [Pa^{-1}]	stress optical coefficient
D [m]	bubble diameter
ε [-]	strain
$\dot{\varepsilon}$ [s^{-1}]	uniaxial elongation rate
I [-]	light intensity
L [m]	distance from bubble surface
N_1 [Pa]	first normal stress difference
t [s]	time
T [s]	period
δ' [nm]	retardation
$\boldsymbol{\Delta n'}$ [-]	refractive index tensor
$\boldsymbol{R}$ [-]	rotation tensor
χ [-]	orientation angle
$\boldsymbol{\varphi}$ [-]	principle azimuthal angle
$\dot{\gamma}$ [s^{-1}]	shear rate
η [Pa·s]	shear viscosity
η_0 [Pa·s]	zero-shear viscosity
η^* [Pa·s]	complex viscosity
λ [m]	wave length
$\boldsymbol{\sigma}$ [Pa]	stress tensor
ξ [-]	non-dimensional distance
ζ [m]	light pass length
ω [rad/s]	angular rate

Subscripts and Superscripts

con	contraction
eq	equivalent
exp	expansion
H	horizontal
V	vertical

is present in the negative wake of a larger bubble. They used direct numerical simulation (DNS) of the transient bubble for a viscoelastic fluid. The vortex ring located at the bottom of the bubble produces a negative wake, which was in agreement with the experimental result. Handzy and Belmonte [11] reported birefringent images of the negative wake behind a bubble rising in a wormlike micellar fluid, an aqueous solution of cetyl-pyridinium chloride and sodium salicylate (CPCl/NaSal). They showed that the residual stress in the tail of the cusped bubble by the crossed Nicols photographs. Belmonte [12] observed the motion of a rising cusped bubble in wormlike micellar aqueous solution of cetyltrimethyl ammonium bromide and sodium salicylate (CTAB/NaSal) in the rotating toroidal cell, and found that the cusp-tip of the bubble is periodically elongated in the vertical direction for larger bubbles. The bubble shape appears to have a knife-edge shape [5,13] in the shortest cusp-tip. The frequency of the oscillation varied slightly and increased with the bubble volume, which Belmonte referred to as bubble self-oscillation. Imaizumi et al. [14] used a new method of mesh deformation tracking and suggested that the cusped shape is related to the release of accumulated elastic energy from shear strain in the viscoelastic fluid.

Theoretical studies on nonlinear oscillations of bubbles in viscoelastic fluids subject to a pulsating pressure is one of the important themes related to ultrasonic cavitation. Fogler and Goddard [15] presented a numerical analysis with regard to collapse of a spherical cavity in a large body of an incompressible linear Maxwell model fluid. Shima et al. [16] theoretically investigated on nonlinear oscillations of gas bubbles in viscoelastic fluids of a three-constant Oldroyd model. Lind and Phillips [17] used boundary element method for a spherical bubble in several differential viscoelastic model fluids such as the Maxwell, the Jeffreys, the Rouse and the Doi-Edwards. The numerical scheme was extended to study the dynamics of non-spherical bubble near a rigid boundary [18] and a free surface [19]. Lind and Phillips [20] also used the spectral element method for the viscoelastic two-phase bubble near the rigid boundary, and showed good agreement with the dynamics observed in other numerical studies along with experimental observations. However, this method suffers from the high Weissenberg number problem. There is a limiting Weissenberg number for each of the fluid models beyond which the simulation fails to converge.

We measured motion of rising bubble under pressure-oscillating field, and reported a significant enhancement of the rising velocity up to approximately 400 times for a shear-thinning fluid with 1–5 mm^3 bubbles in 0.7 wt% aqueous sodium polyacrylate (SPA) [21]. We identified two significant points in this case: (1) In the case of bigger amplitude and higher frequency of pressure-oscillation, the tiny bubble shape changed from spherical to cuspidal when the bubble size reached a minimum during the contraction phase, while the bubble shape became spherical again during the expansion phase. The tiny bubble shape without pressure-oscillation (i.e., natural rising bubble) is spherical due to a very low Reynolds number, such as the order of 10^{-3}, which is much smaller than 1 (Stokes region). (2) A bubble with surrounding fluid undergoes alternating deformation due to bubble expansion and contraction under a pressure-oscillating field, which causes local shear and elongational flow around the bubble. The local shear rate on the surface of isotropically compressing/expanding bubble can be estimated according to the spherical model [21]. The shear rate on the bubble surface was reported to reach up to the order of several hundred, which indicates a sufficient decrease in shear viscosity and the generation of elastic stress. Interestingly, nonuniform radial velocities were observed around the bubble by measurement of motion of a sheet of fine pigments. The radial velocities were high in the lower region of the bubble than the upper region, because the fluid in upper region was surrounded by the rigid cell wall and the fluid was pressed from the downside through a sheet of rubber [22]. Such difference was boosted in the cuspidal bubble shape. The reason of cyclical change between spherical and cuspidal has not been identified in detail, however, should be related with the rheological property and local flow of the surrounding fluid. In this work, the local flow structure around a tiny bubble under a pressure-oscillation field is studied with both high time and space resolution using 2D polarization measurements by which the stress field can also be measured.

2. Experimental

2.1. Test solution

A mixed solution of 0.03 M CTAB and 0.23 M NaSal was used. The solute was dissolved in distilled water using high-performance liquid chromatography. CTAB/NaSal *aq.* exhibits strong flow birefringence due to worm-like micelle orientation under stress conditions [23,24]. This solution is known to obey the stress-optic rule. Fig. 1 shows the rheological properties of the CTAB/NaSal solution, where η is the shear viscosity, N_1 is the normal stress, $|\eta*|$ is the complex viscosity, $\dot{\gamma}$ is the shear rate, and ω is the angular rate. CTAB/NaSal *aq.* exhibits shear-thinning and viscoelastic properties. These data were measured using a rheometer (RS-600, Thermo Scientific Corp.) with a cone-and-plate of 60 mm diameter and a 2.0° gap angle at 23 °C). η and N_1 were obtained by rotational measurements, and $|\eta*|$ was obtained by oscillational measurements. Both η and $|\eta*|$ plots of viscosity are in good agreement in the lower shear rate region. However, nonlinear behavior in the steady rotation case appeared at shear velocities of over 2 s^{-1}. Density of the liquid was 1015.4 kg/m^3. It has been assumed that the rheological and optical properties are kept constant throughout the experiments under pressure-oscillating field.

2.2. Apparatus

Fig. 2 shows a schematic diagram of the experimental apparatus. A bottle-shaped quartz cell was fixed with an expansion block consisting of connections, a hole for piping, the screw cap and the rubber sheet so as to consistently press against the rubber sheet by a vibrating platform

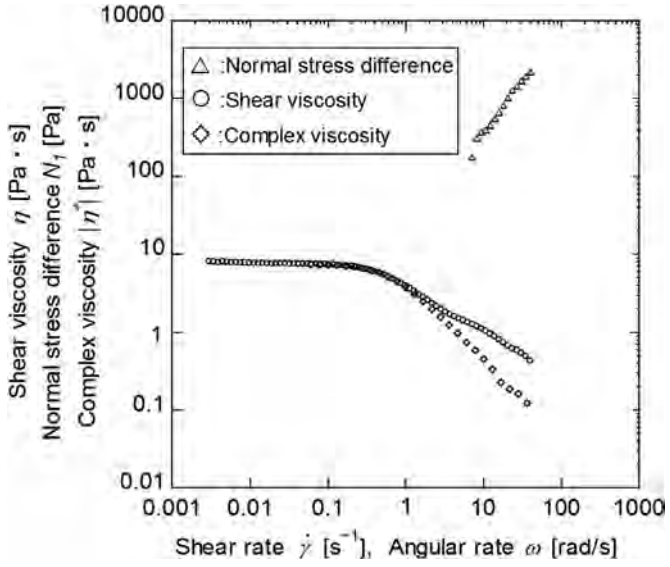

Fig. 1. Rheological behavior of 0.03 M CTAB/0.23 M NaSal *aq*. measured with a rheometer system.

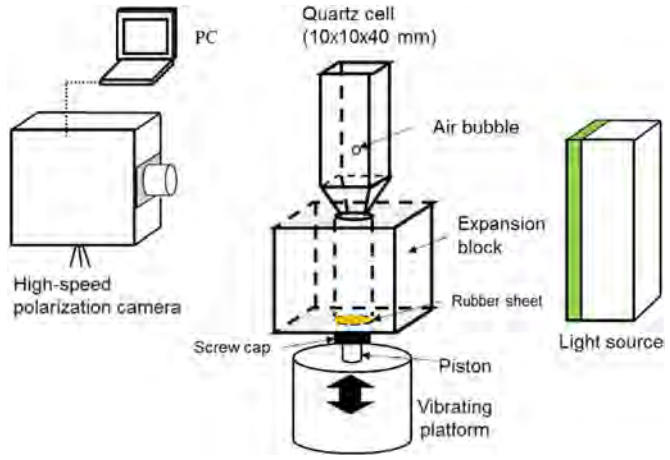

Fig. 2. High-speed polarization camera used to capture the local flow around a tiny air bubble placed in a quartz cell under a pressure-oscillation field.

piston. The cell was filled with CTAB/NaSal *aq.*, that was sealed airtight with the rubber sheet and the screw cap. A tiny air bubble ($V = 5.5$ mm^3) was injected into the lower part of the cell using a microsyringe. The internal size of the cell is $10 \times 10 \times 40$ mm^3. A high-speed polarization camera (CRYSTA PI-1P, Photron Ltd.) was used to capture a square area of 12×12 mm^2. The cell was fixed with an expansion block consisting of connections and a hole for piping so as to consistently press against the rubber of the vibrating platform piston.

The vibrating piston was controlled by a sine-wave generator boosted with a power amplifier system (Wavemaker APA-050FAGO, Asahi Seisakusyo Co. Ltd.), so that the frequency, amplitude, and oscillation center position of the piston could be controlled. The oscillation frequency was fixed at 100 Hz.

2.3. Birefringence measurement

The bubble motion was captured using the high-speed polarization camera. The camera was set up with a resolution of 1024×1024 pixels, a frame rate of 6000 fps, and a 1/6000 s shutter speed. Fig. 3(a) shows a schematic diagram of the optical system used for high-speed polarization imaging. The light source is a green LED with a wavelength of 532 nm that becomes a parallel beam using a collimation lens. The green light passes through linear and circular polarizer films, so that the incident light is circularly polarized. After passing through a sample, the polarized state is changed to elliptical. The camera records the change in the polarization state as a retardation, δ'. A band-pass filter was installed in front of the lens to reduce noise.

Fig. 3(b) shows a schematic diagram of the micro linear polarizer array installed in front of the CCD image sensor. The polarizer array is composed of four pairs of linear polarizers, which are oriented at 45° to the adjacent four pixels. The retardation δ' is calculated from each light intensity (I_1, I_2, I_3, I_4) detected by the image sensor, given as Eqs. (1) and (2) [25]. Therefore, the resolution for polarization imaging is 512×512 pixels. Assuming the validity of the stress-optical rule [26,27] for the local flows around a bubble, the stress tensor $\boldsymbol{\sigma}$, is determined by the refractive index tensor $\Delta \boldsymbol{n}'$, and the inverse of the stress-optical coefficient C, as shown in Eq. (3), where $\boldsymbol{R}$ and χ are the rotation tensor and the rotation angle, respectively. δ' is given by Eq. (4), where ζ is the light path length of the sample, λ is the wavelength, and $\Delta n'_{xy}$ is the component of the refractive index tensor. When supposing a uniform light path length, σ is proportional to δ'. This study shows the presence of the pressure field by measurement of the retardation. Finally, the principle azimuthal angle, φ is given by Eq. (5).

$$\delta' = \sin^{-1} \frac{\sqrt{(I_3 - I_1)^2 + (I_2 - I_4)^2}}{I_0} \tag{1}$$

$$I_0 = \frac{I_1 + I_2 + I_3 + I_4}{2} \tag{2}$$

$$\boldsymbol{\sigma} = \frac{1}{C} \boldsymbol{R}^{-1}(\chi) \boldsymbol{\Delta n'} \boldsymbol{R}(\chi) \tag{3}$$

$$\delta' = \frac{2\pi}{\lambda} \zeta \Delta n'_{xy} \tag{4}$$

$$\varphi = \frac{1}{2} \tan^{-1} \frac{(I_3 - I_1)}{(I_2 - I_4)} \tag{5}$$

3. Experimental results and discussion

3.1. Free rising velocity of an air bubble

Fig. 4 shows the free rising velocity of a tiny air bubble. In this study, the equivalent bubble diameter D_{eq}, was calculated with consideration of the axial symmetry of the cusped bubble, given as Eq. (6), where D_H and D_V are the horizontal and vertical bubble diameters, respectively. The velocity jump is observed around a bubble diameter of $D_{eq} = 3$ mm. For small bubbles ($D_{eq} < 3$ mm), the flow around the bubble is similar to the creep flow. Moreover, before and after the velocity jump, the bubble shape is changed from spherical to oblong and cuspidal.

$$D_{eq} = \sqrt[3]{D_H{}^2 D_V} \tag{6}$$

3.2. Bubble motion under pressure-oscillation field

Pressure oscillation at 100 Hz was applied to a bubble. The rising velocities of a bubble at various diameters are plotted in Fig. 4. It was found that a bubble rising velocity under pressure-oscillation is higher than the natural rising velocity for a bubble with the same diameter. For example, the bubble ($D_{eq} = 2.1$ mm) rising velocity was 0.97 mm/s in Fig. 4. This constitutes an approximately sevenfold higher rising velocity compared with the natural rising velocity for a bubble with the same diameter. A time series variation of D_H and D_V is plotted in Fig. 5(a), where the frame rate is 6000 fps, i.e., 60 video frames can be captured during a period of bubble expansion and contraction. The horizontal axis is non-dimensional time t/T, normalized according to a cycle of

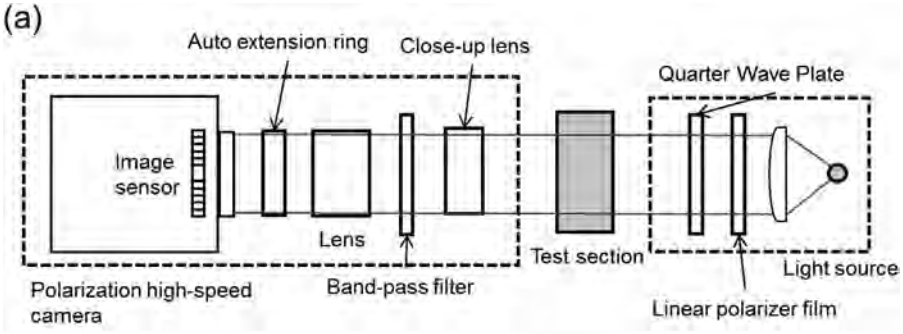

Fig. 3. (a) Schematic diagrams of the optical system for high-speed polarization imaging, and (b) the high-speed polarization image sensor. A micro linear polarizer array consisting four pairs of linear polarizers is attached to the sensor. The maximum resolution for an image is 1024 × 1024.

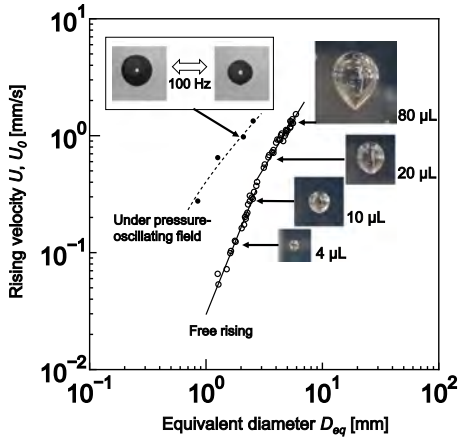

Fig. 4. Change in the rising velocity and bubble shape as the equivalent bubble diameter increases. (○: free rising velocity without pressure-oscillation, U_0 [mm/s]) The free rising bubble shape is spherical without pressure-oscillation; however, the bubble shape changes from spherical to oblong and cuspidal with enhancement of the bubble rising velocity (•: U [mm/s]) under a pressure-oscillation field at 100 Hz.

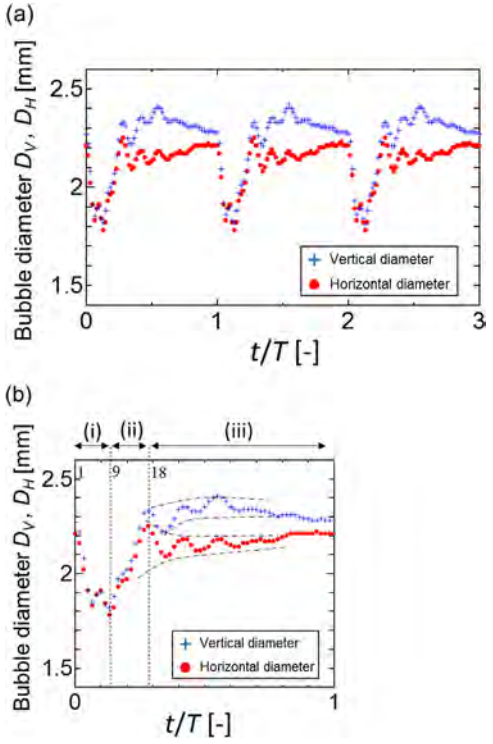

Fig. 5. (a) Periodic changes in the vertical D_V and horizontal diameters D_H over three periods. (b) Bubble motion of the first cycle. The motion can be divided into three phases; (i) contraction phase, Nos. 1–9, (ii) expansion phase, Nos. 10–18, and (iii) idle phase, Nos. 19–60.

pressure oscillation. The bubble diameter changes periodically during a cycle with a gear-tooth-like feature appearing due to performance limitations of the vibrating platform. It may be because of the rubber sheet being inadequately respondent to the piston attached to the vibrating platform. Fig. 5(b) shows a close-up of the first cycle ($0 < t/T < 1$). Let us focus on the sudden change in the bubble diameter; images from Nos. 1 to 9 indicate the bubble contraction phase (i), and those from Nos. 9 to 18 indicate the expansion phase (ii). After expansion, from Nos. 18 to 60 indicate the idle phase (iii). Therefore, rapid expansion produces a slight change in the oscillation of bubble diameter and the oscillation is slowly dampened. Fig. 6 shows the original gray images during each phase. The bubble shape has a cusped shape with a cuspidal point at the bottom of the bubble during the contraction phase.

3.3. Retardation distribution

Fig. 6 also shows the extracted snapshots for the retardation distribution map around the bubble. The entire video images are given as a supplemental file (video 1). The color map indicates retardation with

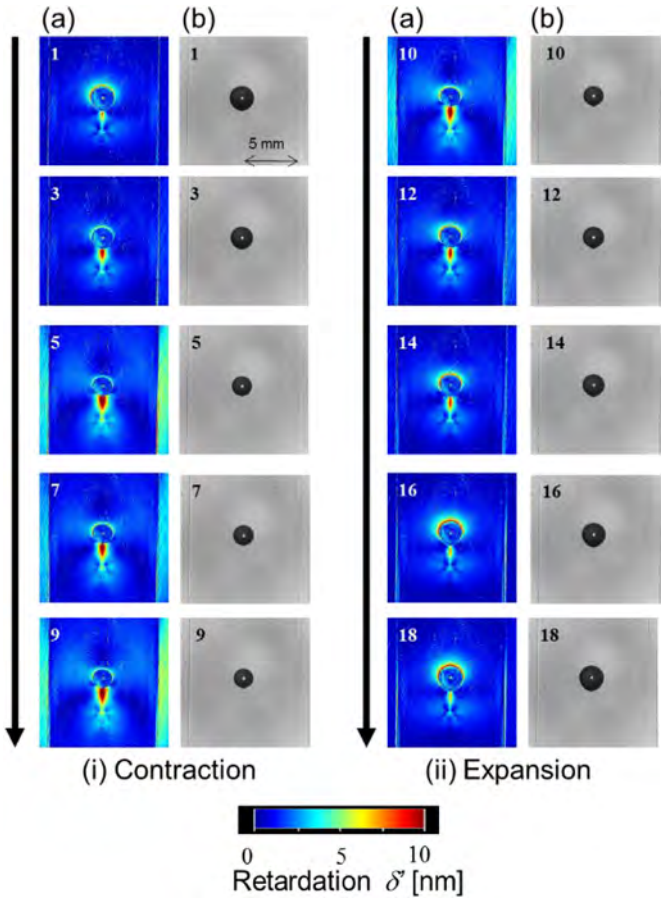

Fig. 6. (a) Periodic change of the retardation distribution during the contraction and expansion phases. Strong vertical retardation due to the orientation of worm-like micelles occurs as a result of local stress at the tail of the bubble during the contraction phase, and a weak retardation occurs near the bubble surface due to biaxial deformation of the surrounding fluid during the expansion phase, (b) Periodic change of original gray images in each phase. The entire video is given as a supplemental file (video 1).

a scale of 0–10 nm, the range of which indicates a strong stress range. Note that the retardation map provides a summation of the local stresses of the test fluid where the transmitted beam passed through. Therefore, this color map is not exactly the same as the axisymmetric stress distribution around the bubble. During the contraction phase (i), strong retardation is observed at the lower side of the bubble. As the bubble contracts, the retardation distribution extends downwards. Both sides of each picture show the cell walls where weak retardation is generated. It is assumed that the internal pressure increased in the quartz cell causing birefringence and finally the retardation was observed. During the expansion phase (ii), the lower part of the retardation disappears gradually. At the same time, the strong retardation distribution spreads around a thin region at the upper side of the bubble. During the natural rising phase (iii), the retardation distribution remains unchanged due to the residual stress.

Fig. 7 shows that the evaluated retardation is dependent on the distance from the bubble surface in each phase (Nos. 1, 9, 18). In the beginning, we focused on the lower side of the bubble, as shown in Fig. 7(a). Here, ξ is a non-dimensional distance which is the distance from the bubble surface L, normalized according to the equivalent diameter, D_{eq}, as shown in Eq. (7). ξ is zero at the bubble surface. Comparison of each phase indicates the maximum contraction phase (No. 9) produces the strongest retardation. Furthermore, the strongest retardation is caused in the vicinity of the bubble surface ($\xi = 0$) and is attenuated with an increase of the distance from the bubble surface, i.e., the retardation value increases exponentially close to the bubble surface. Next, we focused on the upper side of the bubble, as shown in Fig. 7(b), which also shows the strongest retardation in the vicinity of the bubble surface. The after expansion (No. 18) produces the strongest retardation.

From the features of the retardation distribution for each phase, the following two points are inferred: (1) During contraction, deformation as uniaxial elongation occurs at the lower side of the bubble, where the fluids around the lower side of the bubble are elongated momentarily due to the local flow. (2) During expansion, deformation as biaxial extension occurs at the upper side of the bubble, where the fluids around the upper side of the bubble are momentarily extended plate-like due to expansion of the bubble interface.

These deformations are repeated at 100 Hz, so that a stress field is generated periodically in the vicinity of the bubble surface, accompanied by surface deformation. These results correspond to local flow structure around the bubble. The details are discussed in the next section.

$$\xi = \frac{L}{D_{eq}} \tag{7}$$

3.4. Shear rate around the bubble

For shear-thinning fluids, the cyclic change in the bubble diameter induced by the oscillating pressure generates a continuous strong local flow near the bubble surface. It is possible to evaluate the shear rate that occurs in the fluid around the bubble using the spherical model [21], given as Eqs. (8)–(10), where u and $\boldsymbol{S}$ are the radial velocity and the rate of deformation tensor, respectively. The shear rate was evaluated as 595 s^{-1} in this experiment. Here, considering the rheological behavior (Fig. 1), the shear rate corresponds to the region that appears to have low viscosity and high elasticity, which implies a distinct change in the rheological properties in the vicinity of the bubble.

$$\dot{\gamma} = \sqrt{2\boldsymbol{S} : \boldsymbol{S}} = \sqrt{2u_r{}^2 + 4\frac{u^2}{\left(\frac{D_{eq}}{2}\right)^2}} \tag{8}$$

$$u = \frac{dr}{dt} = \frac{d\,D_{eq}}{2dt} = \lim_{\Delta t \to 0} \frac{D_{eq\_\exp} - D_{eq\_con}}{2\Delta t} \tag{9}$$

$$u_r = \frac{du}{dr} = \lim_{\Delta t \to 0} \frac{1}{\Delta t}\left[\left(\frac{D_{eq\_\exp}}{D_{eq\_con}}\right)^2 - 1\right] \tag{10}$$

3.5. Orientation angle

Fig. 8 shows the snapshots for (a) the retardation, (b) grey image, (c) the orientation angle distribution of fluid around the bubble. The color of a plot on the orientation angle map, which corresponds to the angle of the circle color map at the bottom of Fig. 8, indicates the normal direction of the principle azimuthal angle. In the case of expanding bubble, the worm-like micelle is oriented in a circumferential direction around the expanded bubble, as shown in the lower part of Fig. 8(c), which is consistent with the biaxial extensional flow as shown in the lower part of Fig. 8(d). Here, colors of the arrows correspond to the orientation angle. In the case of expanding bubble, however, the vertical orientation can be seen below the contracting bubble surface as shown in the upper part of Fig. 8(c). A uniaxial extensional flow as well as oblique inflow in the contraction phase can be described as the upper part of Fig. 8(d). The vertical orientation can also be seen even in the expansion phase. The strong retardation still remained over a cycle. This implies a distinct change in the rheological properties in the lower vicinity of the bubble.

3.6. Local flow model

Bubbles generally maintain their spherical shape due to surface tension. When a weak pressure is applied, the bubble also remains spherical

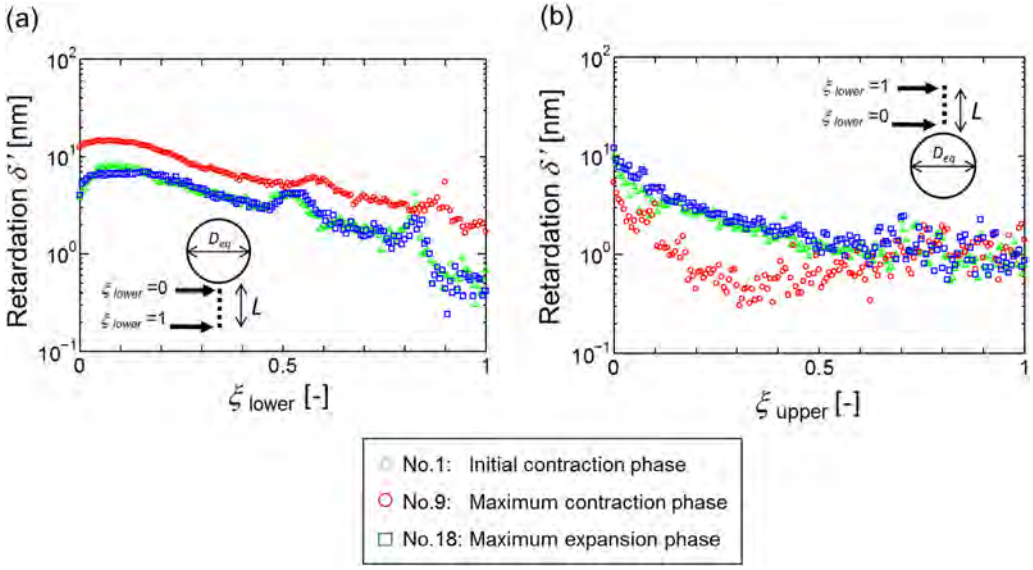

Fig. 7. Effect of non-dimensional distance ξ on (a) upper retardation and (b) lower retardation. Nos. 1, 9 and 18 show the initial contraction phase, the maximum contraction phase, and the maximum expansion phase, respectively. During the maximum contraction phase, strong retardation is observed at the tail of the bubble, whereas it is attenuated faster at the top of the bubble, which indicates that the more complex flow occurs in the region behind the bubble.

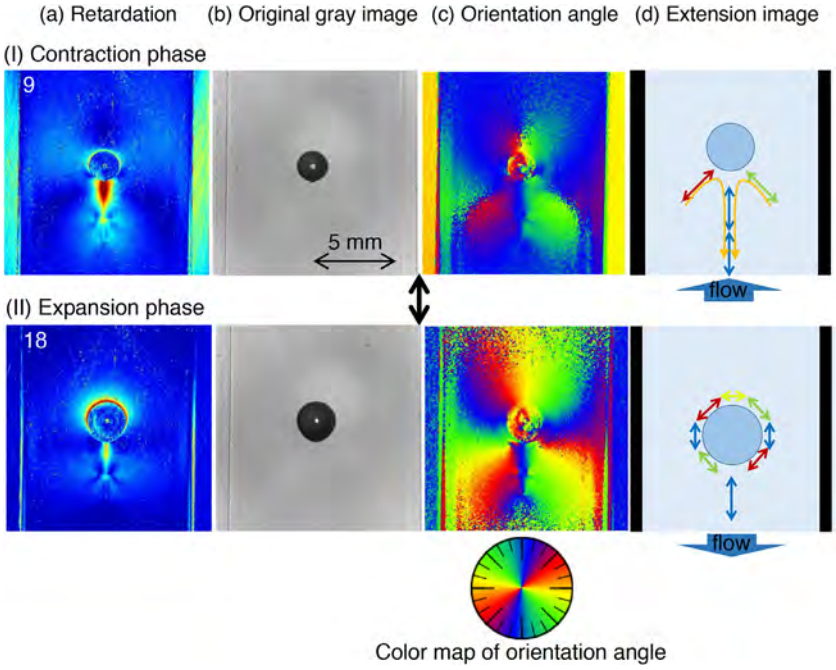

Fig. 8. (a) retardation maps, (b) original gray image, (c) orientation angle map, and (d) schematic image of extensional direction, at No.9 (contraction phase) and No.18 (expansion phase). The circle map indicates a color map of the orientation angle. The vertical orientation can be seen at the lower part of bubble in the contraction phase. In the expansion phase, the circumference orientation was observed around the bubble surface.

because the bubble is being pressured isotropically. However, instantaneous deformation by expansion and contraction was applied to the bubble in a viscoelastic fluid using a pressure oscillation. In this case, local flow occurs around the bubble, and the effect of elasticity is greater than the restorative force due to surface tension. In addition, we considered the local flow structure of cusped shape.

When the bubble changes from expansion to contraction, the bubble volume decreases and the fluid flows in to fill the vacant space. We may refer to this supply flow as inflow. Fig. 9 shows the flow structure of the cusped shape during the contraction phase. In the contraction phase, inflow is concentrated around the lower part of the bubble, but then starts to flow towards the lower direction. These local flows are consistent with the maps of orientation angle as shown in Fig. 8. Here, hoop stress occurs along the edge of the bubble. As a result, the bubble exhibits a cusped shape.

3.7. Local flow visualization

To confirm the predicted flow, a flow visualization experiment was prepared using tracer particles (hollow glass, 40 μm particle diameter, specific gravity 0.998–1.002), laser sheet, and the high-speed polarization camera. A green laser light was used as the light source and passed through cylindrical and convex lenses. The sheet was irradiated from the side of the cell to the vertical cross-section of the bubble, which enables visualization on the same plane. Fig. 10 shows the resultant deformation. The trajectory and contour of the bubble shape and the

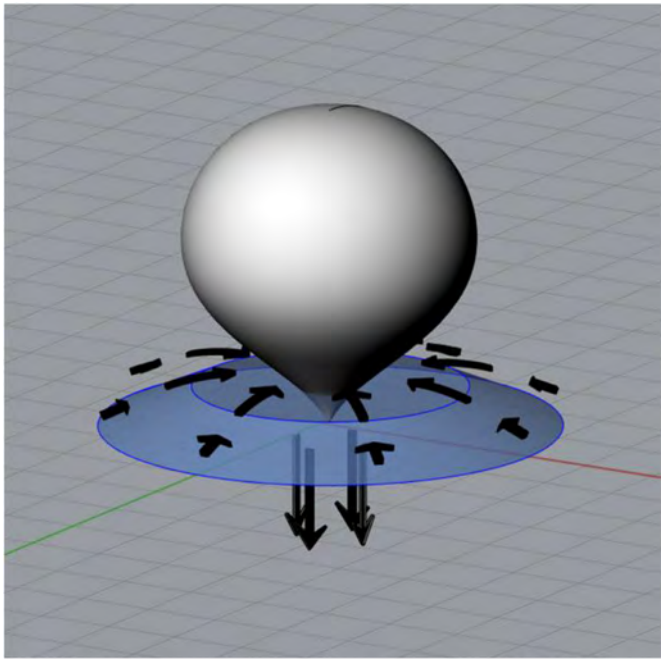

Fig. 9. Flow model that predicts the bubble surroundings during the contraction phase. The inflow appears umbrella-like due to a reduction of the bubble surface area. The inflow surrounding the bubble starts to flow in the lower direction as outflow.

target tracer at consecutive contraction phases are plotted in scale. The combined frames captured at consecutive contraction phases are given as a supplemental file (video 2). The bubble size is 4 mm^3 with a diameter of 2.0 mm. t/T indicates the snapshot number at the time of the contraction phase. As the bubble rises, the tracers move to the upper direction ($1 < t/T < 6$). The tracers move downwards after $t/T = 6$ and the downward flow becomes weaker as the distance from the bubble edge increases. The distance between the tracer and the bubble edge during the contraction phase L_{con}, is plotted in Fig. 11.

In addition, the Hencky strain ε, and the uniaxial elongation rate $\dot{\varepsilon}$, were calculated using Eqs. (11) and (12). $\dot{\varepsilon}$ is plotted in Fig. 11 as the second axis. $\dot{\varepsilon}$ is suddenly attenuated with the increase in L_{con} when the tracer is away from the bubble edge. However, the slope decreased after $t/T = 18$, which implies that the tracer traveled along the strong local uniaxial elongation region at the tail of the bubble at the maximum of the contraction phase. The result is in agreement with the birefringence profile and the local flow model described in Fig. 9.

$$\varepsilon = \ln \frac{L_{con}}{L_{\exp}} \tag{11}$$

$$\dot{\varepsilon} = \frac{L_{con} - L_{\exp}}{L_{\exp} dt} \tag{12}$$

3.8. Effect of frequency on the bubble motion

The upper figures of Fig. 12 show an effect of frequency on the flow structure around the bubble under the pressure-oscillating field from 50 to 300 Hz. The amplitude of vibrating platform was kept fixed in these experiments. As pressure-oscillation frequency is increasing, stronger retardation can be seen at the lower part of the bubble during the contraction phase. Note that due to the mechanical limitation of the vibrating platform, the condition of pressure-oscillation was tuned properly for 300 Hz operation. As pressure-oscillation is applied at higher frequency, the rising velocity of bubble is getting accelerated from about 4 to 7 times compared to its free rising velocity without pressure-oscillation. The retardation color map with the bigger vibration amplitude at 100 Hz

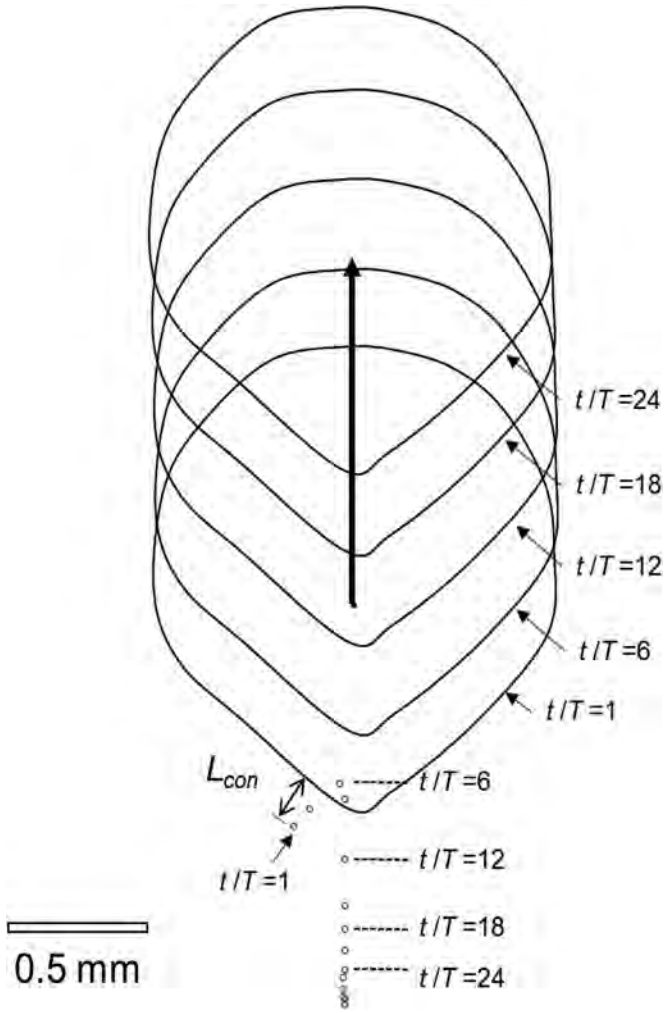

Fig. 10. Positional relationship between the tracer and bubble. L_{con} [mm] is the distance from bubble surface edge to the tracer during the contraction phase (in scale). The tracer moves towards the cusp-tips and then after approaching the tracer moves rapidly downward. The combined frames captured at consecutive contraction phases are given as a supplemental file (video 2).

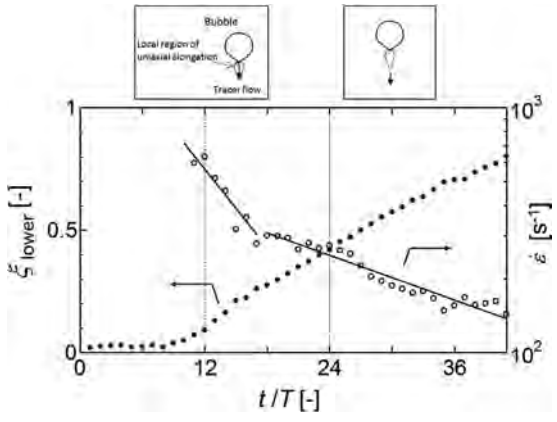

Fig. 11. Trajectory of the tracer position L_{con}, and the uniaxial elongational rate, $\dot{\varepsilon}$. $\dot{\varepsilon}$ is rapidly attenuated with the distance ξ in the local region of uniaxial elongation.

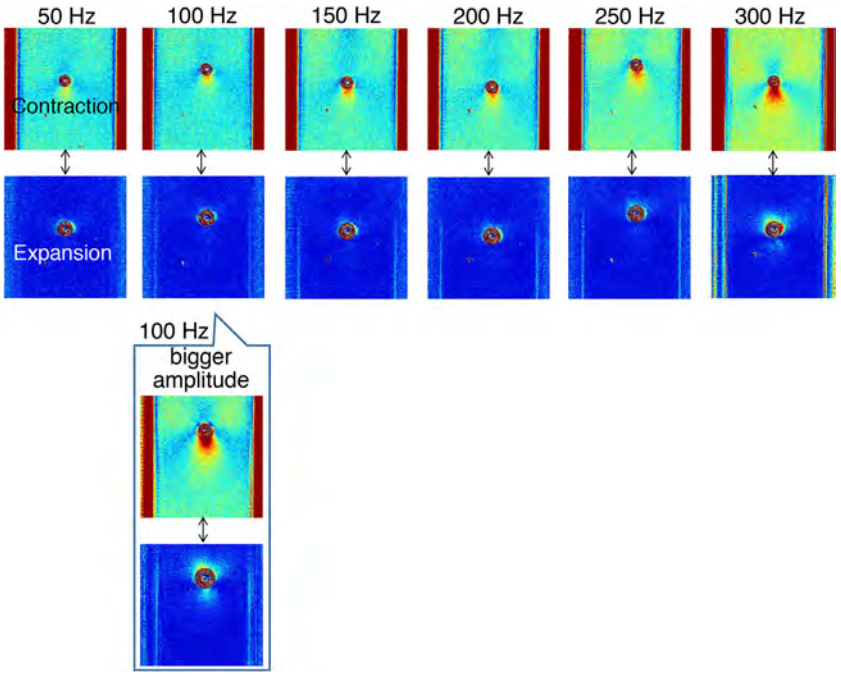

Fig. 12. The evaluated retardation distribution from 50 to 300 Hz in the contraction phase and expansion phase, respectively. In the contraction phase, the stronger retardation was observed at higher frequency. When the bigger vibrating amplitude was applied to the system at 100 Hz, the stronger retardation was observed as shown in the lower part.

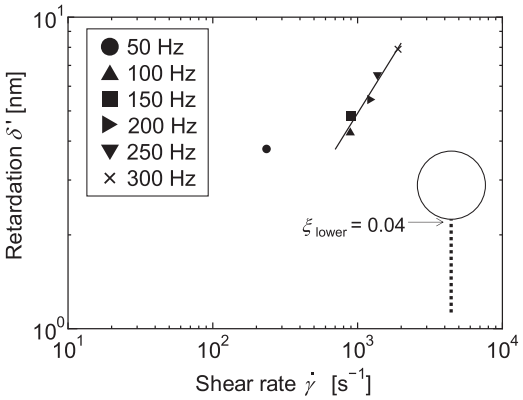

Fig. 13. The enhanced retardation at the contraction phase and shear rate is plotted at each frequency. The shear rate is calculated for changing the distance of bubble expanded and contracted from bubble surface to one position ($\xi = 0.04$). The retardation is proportion to frequency at 100–300 Hz.

was given at the lower part of Fig. 12. With increasing amplitude of pressure-oscillation, the stronger retardation also can be seen at the lower part of the bubble during the contraction phase.

Fig. 13 shows a dependence of the local shear rate on retardation at the lower vicinity of the bubble ($\xi = 0.04$). The local shear rate on the surface of the bubble can be estimated by Eq. (8). Depending on the frequency and the change in bubble diameter under pressure-oscillating field, the local shear rates on the bubble surface were calculated in order of 100–2000 [1/s] as shown in Fig. 13. When we have considered the liquid rheological behavior in Fig. 1, such higher shear rate indicates non-linear behavior of the fluid. The shear viscosity using cone and plate flow geometry and the complex viscosity using sinusoidal oscillating cone and plate flow geometry are different from each other, as well as strong normal stress difference could be seen. Ouchi et al. [28] showed that the Shear Induced Structure (SIS) of the test fluid can be generated over strain of 4–7 [−]. The relaxation time of the SIS fluid may be much longer than the relaxation time of the original fluid. In our experiments, strains surrounding the bubble were smaller than the values of less than about 0.5. As the SIS condition may not be generated in the vicinity of the bubble under pressure-oscillating field, the clear cyclical 2D retardation images can be obtained throughout experiments.

4. Conclusions

The shape of a tiny bubble in CTAB/NaSal *aq*. was observed under a pressure-oscillating field. For free rising, the shape changes from spherical to a cusped shape as the bubble size increases. In this case, the critical volume is approximately $V = 14$ mm^3 with $D_{eq} = 3$ mm, the rising velocity of the bubbles can be accelerated by applying pressure-oscillation. A tiny bubble ($V = 5.5$ mm^3, $D_{eq} = 2.2$ mm) showed a cusped point at the tail and the rising velocity was accelerated by nearly seven-fold during the contraction phase under the pressure-oscillation field. 2D polarization measurement was conducted to investigate the deformation of the fluid under a pressure-oscillation field. These results including the orientation distributions indicated that deformation as uniaxial extension occurred at the tail of the bubble during the contraction phase as well as the biaxial extensional deformation occurred at the upper side of the bubble. In addition, a local flow visualization experiment using tracer particles was conducted to investigate the flow structure around the bubble. It was revealed that a negative wake occurs at the tail of the bubble due to rapid deformation of the bubble surface, and the negative wake produces deformation as uniaxial extension of the bubble.

Acknowledgements

The authors would like to thank Mr. Akinobu Nakayama and Mr. Hikaru Horiuchi for performing the birefringence high speed imaging experiments. The authors also would like to thank Ms. Akiko Onishi for technical assistance with the experiments. This work was supported by JSPS KAKENHI Grant Numbers (Nos. 23560195, 26420107, 17K06152) from the Japan Society for the Promotion of Science (JSPS).

Supplementary materials

Supplementary material associated with this article can be found, in the online version, at doi:10.1016/j.jnnfm.2018.11.002.

References

[1] R.P. Chhabra, Bubbles, Drops, and Particles in Non-Newtonian Fluids, 2nd ed., CRC Press, Florida, 2007.
[2] G.G. Stokes, On the effect of the internal friction of fluids on the motion of pendulums, *Trans. Cambridge Philos. Soc.* 9 (1851) 8–106.
[3] G. Astarita, G. Apuzzo, Motion of gas bubble in non-Newtonian liquid, AIChE J 11 (1965) 815–820.
[4] J.S. Hadamard, C.R. Hebd. Seances Acad. Sci. 152 (1911) 1735–1738.
[5] O. Hassager, Negative wake behind bubbles in non-newtonian liquids, Nature 279 (1979) 402–403.
[6] J.R. Herrera-Valarde, R. Zenit, D. Chehata, B. Mena, The flow of non-Newtonian fluids around bubbles and its connection to the jump discontinuity, J. Non-Newtonian Fluid Mech. 111 (2003) 199–209.
[7] D. Funfschilling, H.Z. Li, Flow of non-Newtonian fluids around bubbles PIV measurements and birefringence visualization, Chem. Eng. Sci. 56 (2001) 1137–1141.
[8] H.Z. Li, Bubbles in non-Newtonian fluids: Formation, interactions and coalescence, Chem. Eng. Sci. 54 (1999) 2247–2254.
[9] M. Kemiha, X. Frank, S. Poncin, H.Z. Li, Origin of the negative wake behind a bubble rising in non-Newtonian fluids, Chem. Eng. Sci. 61 (2006) 4041–4047.
[10] S.B. Pillapakkam, P. Singh, D. Blackmore, N. Aubry, Transient and steady state of a rising bubble in a viscoelastic fluid, J. Fluid Mech. 589 (2007) 215–252.
[11] N.Z. Handzy, A. Belmonte, Oscillatory Rise of Bubbles in Wormlike Micellar Fluids with Different Microstructures, physics.flu-dyn, 2003, 11 Nov.
[12] A. Belmonte, Self-oscillation of a cusped bubble rising through a micellar solution, Rheol. Acta 39 (2000) 554–559.
[13] Y. Liu, T. Liao, D.D. Joseph, A two dimensional cusp at the trailing edge of an air bubble rising in a viscoelastic liquid, J. Fluid Mech. 304 (1995) 321–342.
[14] Y. Imaizumi, T. Kunugi, T. Yokomine, Z. Kawara, Viscoelastic fluid behaviors around a rising bubble via a new method of mesh deformation tracking, Chem. Eng. Sci. 120 (2014) 167–173.
[15] H.S. Fogler, J.D. Goddard, Collapse of spherical cavities in viscoelastic fluids, Phys. Fluids 13 (1970) 1135–1141.
[16] A. Shima, T. Tsujino, H. Nanjo, Nonlinear oscillations of gas bubbles in viscoelastic fluids, Ultrasonics 24 (1986) 142–147.
[17] S.J. Lind, T.N. Phillips, Spherical bubble collapse in viscoelastic fluids, J. Non-Newtonian Fluid Mech. 165 (2010) 56–64.
[18] S.J. Lind, T.N. Phillips, The influence of viscoelasticity on the collapse of cavitation bubbles near a rigid boundary, Theor. Comput. Fluid Dyn. 26 (2012) 245–277.
[19] S.J. Lind, T.N. Phillips, The effect of viscoelasticity on the dynamics of gas bubbles near free surfaces, Phys. Fluids 25 (2013) 022104.
[20] S.J. Lind, T.N. Phillips, Bubble collapse in compressible fluids using a spectral element marker particle method. Part 2. Viscoelastic fluids, Int. J. Numer. Meth. Fluids 71 (2013) 1103–1130.
[21] S. Iwata, Y. Yamada, T. Takashima, H. Mori, Pressure-oscillation deforming for viscoelastic fluid, J. Non-Newtonian Fluid Mech. 151 (2008) 30–37.
[22] S. Iwata, Y. Yamada, S. Komori, H. Mori, Experimental visualization of local flow of shear-thinning fluid around a small bubble for pressure-oscillating defoaming, Kagaku Kogaku Ronbunshu 34 (2008) 417–423.
[23] T. Shikata, S.J. Dahman, D.S. Pearson, Rheo-optical behavior of wormlike micelles, Langmuir 10 (1994) 3470–3476.
[24] T. Takahashi, G. Fuller, Stress tensor measurement using birefringence in oblique transmission, Rheol. Acta 35 (1996) 297–302.
[25] T. Onuma, Y. Otani, A development of two-dimensional birefringence distribution measurement system with a sampling rate of 1.3 MHz, Opt. Commun. 315 (2014) 69–73.
[26] GeraldG. Fuller, Optical Rheometry of Complex Fluids, Oxford University Press, 1995.
[27] R.S. Sirohi, F.S. Chau, Optical Methods of Measurement: Whole Field Techniques, Marcel Dekker, 1999.
[28] M. Ouchi, T. Takahashi, M. Shirakashi, Rheological properties of shear-induced structure in CTAB/NaSal aqueous solution, Nihon Reoroji Gakkaishi 35 (2007) 107–114.